ISSN 1063-7710, Acoustical Physics, 2018, Vol. 64, No. 6, pp. 731–741. © Pleiades Publishing, Ltd., 2018.

ATMOSPHERIC AND AEROACOUSTICS

Convolution Quadrature Time-Domain Boundary Element Method for Two-Dimensional Aeroacoustic Noise Prediction[1]

Xinzhong Gu[a, b, *] and Shunming Li[a]

[a] *College of Energy and Power Engineering, Nanjing University of Aeronautics and Astronautics, Nanjing, 210016 China*

[b] *Department of Vehicle Engineering, Nanhang Jincheng College, Nanjing, 211156 China*

**e-mail: guxingzhong007@126.com*

Received October 14, 2017

Abstract—The computation of a compressible flow for aeroacoustic prediction is a challengeable work insofar as the fluctuation is usually very small in a sound field compared with the flow field. For the low Mach number considered in this study, a discrete vortex method in conjunction with fast multipole time-domain boundary element method is developed and applied to predict far-field sound resulting from a 2D vortex dominated flow. The flow field is simulated employing the classical discrete vortex method. The sound field scattered by solid bodies is determined by using a time-domain boundary element method combined with the convolution quadrature approach, by means of which the convolution integral is approximated by a quadrature formula utilizing a Laplace-domain fundamental solution. In addition, the fast multipole method is applied to improve the computational efficiency. Finally, several examples are presented to check the applicability and accuracy of the method. Numerical results indicate that the noise predicted by the present method agrees well with the experimental results, and the sound pressure levels of the cylinder models have a dipole-like directivity at vortex shedding frequency.

Keywords: Discrete vortex method, convolution quadrature method, fast multipole method, time-domain boundary element method, aeroacoustic noise

DOI: 10.1134/S1063771018060027

1. INTRODUCTION

Aeroacoustic sound is an important issue in several technical applications, including wind turbine noise, rotor craft [1] and fan noise [2]. This noise is generated by fluctuations of the vortical flow or by directly converting the vortical energy into sound in the near field, which is associated with pressure fluctuations that propagate to the far field.

The complicated unsteady vortical flow, which is actually the source of an aeroacoustic sound, is related to the compressibility of air and needs to be calculated based on the compressible Navier–Stokes equations. At present, these equations can be numerically solved using the computational aeroacoustics method (CAA), allowing an investigator to determine what the noise generation mechanisms and sound propagation processes are and to obtain a better understanding of the physics of these problems [3, 4]. Note that aeroacoustic problems typically involves wide bandwidth and long propagation distances; furthermore, the amplitude of sound pressure is usually very small compared with the mean flow. That means the CAA method needs to adopt high-order finite difference schemes to reduce numerical noise and to minimize numerical dispersion and dissipation [5, 6]. That will lead to the computation time and memory increasing drastically, and limit the CAA to be used in general [7].

An alternative method to the CAA (called splitting method) is to split the problem into source mechanism and sound propagation. The source region governed by full nonlinear equations is computed using computational fluid dynamics techniques (CFD) [8, 9]. The sound source terms are extracted using the near-field results, according to the Ffowcs Williams and Hawkings (FWH) equation [10, 11]. Then the far-field sound can be calculated by solving an inhomogeneous wave equation [12].

Although the splitting method can save computational time and memory storage compared with the CAA, it involves some difficulties:

1. Very fine grids are usually required, since they are directly related to the lowest resolvable scale and thus to the highest frequency which is accurately represented.

2. Due to the large range of spatial and time scales present in turbulent flows, CFD techniques are very time-consuming in obtaining high-frequency flow field quantities for aeroacoustics predictions [13].

[1] The article is published in the original.

3. With complicated geometries, it is not feasible to analytically construct a Green's function. Further, restrictions need to be put on the size of the surface (compact source) to extract acoustic signals [14].

In conclusion, the splitting method still remains expensive for practical applications. A possible way to avoid the issues is to obtain a simplified formulation by introducing more assumptions that are satisfied in most cases. Keep in mind that vorticity is the major mechanism for noise generation [15], thus the choice of the vortex method computation for such problems is very reasonable.

The vortex method can reveal the influence of a surface pressure gradient upon vorticity producing, the nonlinear interactions between shed vortices and the distortions of a vorticity field encountering solid bodies. Clearly, it is not capable of capturing all the important flow features, but is sufficient to provide the information for a far-field sound prediction [16–18].

In the acoustic part, various approaches have been proposed with their numerical simulations for acoustic wave propagation and scattering problems, such as the boundary element method (BEM) [19, 20]. aeroacoustic problems usual with moving sound sources or vibrating surfaces are by definition time dependent, thus it is better to solve them using a time-domain BEM. However, the time-domain simulations are relatively less studied due to the instability in time stepping procedure. Besides numerical instability, the time-domain boundary element method (TDBEM) needs a fundamental solution, which is not available for those complex problems [21]. Addressing this issue, the convolution quadrature method (CQM), which was pioneered by Lubich [22, 23], has been developed as a technique to approximate convolution integrals. Then, a new time-stepping procedure can be established without the knowledge of the time-domain fundamental solutions. Additionally, the resulting quadrature formula can improve the stability behavior of a time-stepping procedure [24]. Although the convolution quadrature boundary element method (CQ-BEM) is a powerful tool for analyzing wave propagation, it fails to solve large-scale acoustic problems due to the high computational cost. To improve computing efficiency, the fast multipole time-domain boundary element method (CQ-FMBEM), combined with the TDBEM, CQM and the fast multipole method (FMM), has been developed for solving large-scale problems [21, 25].

However, no such CQ-FMBEM for aeroacoustic noise computation has yet been proposed. In this work, we develop a new numerical method, which is integrated with the discrete vortex method (DVM), CQ-BEM and FMM, for the aeroacoustic sound prediction. The DVM coupled with vortex sound equation is applied to obtain the acoustic signals from a flow field, while the TDBEM is used for sound waves scattering analysis. The CQM makes it possible for the TDBEM to calculate waves radiated from numerous moving sound sources and scattered by multiple surface elements. In addition, the FMM helps to overcome the computational efficiency problem.

The article is organized in the following way. A short review on the fundamental equations for flow-induced noise is presented in Sect. 2. In Sect. 3, the basic formulations for DVM, CQ-BEM and FMM are introduced. A description of the CQ-FMBEM algorithm is presented in Sect. 4. In order to validate the formulations and verify the algorithm, three examples are presented and the numerical results are discussed in Sect. 5.

2. GOVERNING EQUATIONS

When a bluff body is placed in a uniform flow, turbulence is typically generated in the boundary layer and in the wake of the flow. Aerodynamic sound arises primarily by vortices shedding and moving in the wake. As a result, to compute flow-induced noise generation, the flow field can be split into an inner domain and an outer domain. The outer domain is essentially irrotational and can therefore be described by means of a velocity potential, while the inner one is typically vortical and should be modeled using compressible Navier–Stokes equations in theory. If the Mach number is considered to be low, the compressibility effect remains small enough. The flow in the inner domain can be approximately described by incompressible Navier–Stokes equations:

$$\frac{\partial \mathbf{u}}{\partial t} + (\mathrm{u}\cdot\boldsymbol{\nabla})\,\mathbf{u} + \frac{1}{\rho_0}\boldsymbol{\nabla} p_0 = \nu\boldsymbol{\Delta}\mathbf{u}, \tag{1}$$

$$\boldsymbol{\nabla}\cdot\mathbf{u} = 0. \tag{2}$$

To research the aerodynamic sound generation, Lighthill proposed an aeroacoustic model by transforming the Navier–Stokes and continuity equations to form an exact, inhomogeneous wave equation [26]:

$$\left(\frac{1}{c_0^2}\frac{\partial^2}{\partial t^2} - \boldsymbol{\nabla}^2\right)\rho = \boldsymbol{\nabla}\cdot\boldsymbol{\nabla} T_{ij}, \tag{3}$$

where $T_{ij} = \rho \mathbf{v}_i\mathbf{v}_j - \sigma_{ij} + \delta_{ij}[(p-p_0) - c_0^2(\rho-\rho_0)]$ is the Lighthill stress tensor, the term $\rho\mathbf{v}_i\mathbf{v}_j$ is the Reynolds stress and σ_{ij} is the viscous stress tensor.

In a low Mach number flow, the acoustic amplitude is very small relative to the mean pressure p_0, the non-linear effect on sound propagation can therefore be ignored. Furthermore, the value of Lighthill's quadrupole source can be approximated by means of its principal component. Then, Eq. (3) is reduced to a much simplified form [14]:

$$\frac{1}{c^2}\frac{\partial^2 p}{\partial t^2} - \boldsymbol{\nabla}^2 p = \rho_0\boldsymbol{\nabla}\cdot(\boldsymbol{\omega}\times\mathbf{u}), \tag{4}$$

where p is the sound pressure, c is the propagation velocity, $\mathbf{u}$ is the velocity field, $\boldsymbol{\omega}$ is the vorticity and ρ_0 is the density of fluid.

A 2D fundamental solution of Eq. (4) in time domain represents the wave propagation in a free space due to an impulse at emission time τ in point $\mathbf{y}$, and is given by

$$G(\mathbf{x},t/\mathbf{y},\tau)=\frac{cH[c(t-\tau)-r]}{2\pi\sqrt{c^2(t-\tau)^2-r^2}}, \tag{5}$$

where $H[\cdot]$ is the Heaviside function, r is the distance between the source point $\mathbf{y}$ and the field point $\mathbf{x}$.

Obviously, the presence of a boundary S will affect the sound field. When the incident wave hits a solid surface, scattered waves are generated, as shown in Fig. 1.

The total waves, sum of the incident wave and scattered waves, can be obtained from the following general representation integral:

$$\begin{aligned}p(\mathbf{x},t)=&\int_0^t\int_S G(\mathbf{x},t/\mathbf{y},\tau)q(\mathbf{y},\tau)\\&-\frac{\partial G}{\partial\mathbf{n}}(\mathbf{x},t/\mathbf{y},\tau)p(\mathbf{y},\tau)dS(\mathbf{y})d\tau\\&-\int_0^t\int_\Omega a(\mathbf{y},\tau)G(\mathbf{x},t/\mathbf{y},\tau)d\Omega(\mathbf{y})d\tau.\end{aligned} \tag{6}$$

Here $q=\partial p/\partial\mathbf{n}$ denotes the sound flux, Ω is the computational domain and a represents the source term. Once the values of both p and q are known on S, Eq. (6) can be used to determine far-field sound pressure.

3. NUMERICAL METHOD

3.1. Discrete Vortex Method

In the inner domain, incompressible Navier–Stokes equations are transformed into the vorticity transport equation:

$$\frac{D\boldsymbol{\omega}}{Dt}=\frac{\partial\boldsymbol{\omega}}{\partial t}+\mathbf{u}\cdot\nabla\boldsymbol{\omega}=(\nabla\mathbf{u})\cdot\boldsymbol{\omega}+\nu\nabla^2\boldsymbol{\omega}, \tag{7}$$

where ν is the kinematic viscosity.

In the DVM, dynamics of fluid motion is studied using a split algorithm [27]:

$$\begin{aligned}\partial\omega/\partial t+\mathbf{u}\cdot\nabla\boldsymbol{\omega}=0,\\ \partial\omega/\partial t=\nu\nabla^2\boldsymbol{\omega},\end{aligned} \tag{8}$$

and the vorticity field is presented by a set of Gaussian smoothing vortex particles:

$$\Gamma(\mathbf{y},t)=\Gamma_i\left(1-e^{-|\mathbf{y}-\mathbf{y}_i|^2/4\nu t}\right). \tag{9}$$

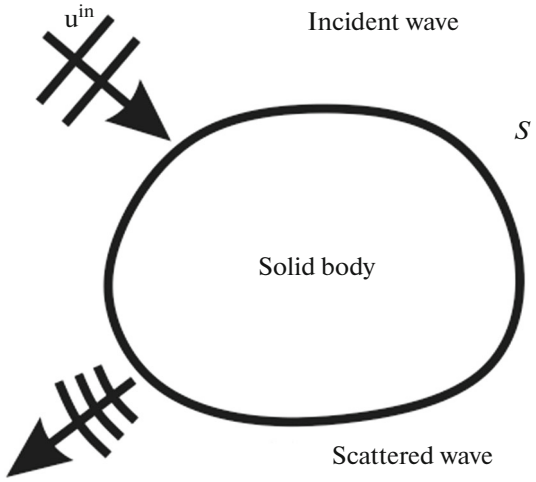

Fig. 1. Wave scattering.

Each particle, characterized by its position $\mathbf{y}_i$ and circulation Γ_i, is created on the body surface to satisfy the no-slip condition [28]:

$$\sum_{n=1}^{M}K(s_m,s_n)\gamma(s_n)=-u_\infty\cos\beta_m-v_\infty\sin\beta_m, \tag{10}$$

where M is the finite number of boundary element, K is the matrix of coupling coefficients, $\gamma(s_n)$ is the strength of surface element s_n, β_m is the profile slope of surface element s_m, u_∞ and v_∞ are the components of inflow velocity parallel to the x and y axes.

Then a first order Euler scheme is used to convect the particles:

$$\mathbf{y}(t+\Delta t)=\mathbf{y}(t)+\mathbf{u}_I(t)\Delta t+\Delta\mathbf{y}, \tag{11}$$

where $\mathbf{u}_I$ is the sum of induced velocity, which can be computed using the Biot–Savart law. In addition, $\Delta\mathbf{y}$ is the random displacement used for the viscous diffusion simulation [28].

Aiming at reducing the number of vortices, the particles are examined at each step pair by pair and will be merged, provided they satisfy the following condition:

$$\frac{|\Gamma_i\Gamma_j|}{|\Gamma_i+\Gamma_j|}|\mathbf{y}_i-\mathbf{y}_j|\le\varepsilon_0, \tag{12}$$

where ε_0 is a prescribed small value [29].

Obviously, the DVM provides time histories of strength and velocity for each vortex particle, which can be used for sound source evaluation on the right-hand side of Eq. (4).

3.2. CQ-BEM Formulation for 2D Scattering Problems

3.2.1. Boundary Integral Equation. To perform time integration for the boundary equation obtained in Sect. 2, the CQM is adopted in this work. Then,

Eq. (6) for a 2D wave propagation problem can be expressed by

$$\frac{p(\mathbf{x},t)}{2} = \int_S G(\mathbf{x},\mathbf{y},t) * q(\mathbf{y},t) - H(\mathbf{x},\mathbf{y},t) * p(\mathbf{y},t)\,dS(\mathbf{y}) - \int_\Omega G(\mathbf{x},\mathbf{y},t) * a(\mathbf{y},t)\,d\Omega(\mathbf{y}), \tag{13}$$

where G and $H = \partial G/\partial \mathbf{n}$ denote the time-domain fundamental solution and its double-layer kernel of the 2D wave propagation equation respectively [30]. In addition, (*) is the symbol of time convolution, defined as

$$f * g(t) = \int_0^t f(t-\tau)\,g(\tau)\,d\tau,\ t > 0. \tag{14}$$

3.2.2. Time Discretization. A fixed time step Δt is adopted, equal to that used in flow field computation. Then, the time axis is $0 = t_0, t_1, \ldots, t_m = m\Delta t = t$. After the boundary discretization is carried out, substituting the quadrature formula (14) into the convolution integrals gives a discrete version of Eq. (13) for boundary node i,

$$\begin{aligned}\frac{p(\mathbf{x}_i, m\Delta t)}{2} &= \sum_{k=0}^{m}\sum_{s=1}^{N}\sum_{j=1}^{M} \omega_{m-k}\left(\hat{G},\mathbf{x}_i,\Delta t\right) q_{js}(k\Delta t) \\ &- \sum_{k=0}^{m}\sum_{s=1}^{N}\sum_{j=1}^{M} \omega_{m-k}\left(\hat{H},\mathbf{x}_i,\Delta t\right) p_{js}(k\Delta t) \\ &- \sum_{k=1}^{m}\sum_{s=1}^{N} \omega_{m-k}\left(\hat{G},\mathbf{x}_i,\Delta t\right) a_s(k\Delta t).\end{aligned} \tag{15}$$

Here N is the number of vortex particle, ω_{m-k} is the quadrature weight, which is obtained from a Laplace transformed fundamental solution using the trapezoidal rule with L equal steps $(2\pi/L)$ [31]:

$$\omega_n\left(\hat{G},\mathbf{x},\Delta t\right) = \frac{\rho^{-n}}{L}\sum_{l=0}^{L-1} \hat{G}\left(\mathbf{x},\mathbf{y},\gamma\left(\frac{\rho e^{il2\pi/L}}{\Delta t}\right)\right) e^{-inl2\pi/L}, \tag{16a}$$

$$\omega_n\left(\hat{H},\mathbf{x},\Delta t\right) = \frac{\rho^{-n}}{L}\sum_{l=0}^{L-1} \hat{H}\left(\mathbf{x},\mathbf{y},\gamma\left(\frac{\rho e^{il2\pi/L}}{\Delta t}\right)\right) e^{-inl2\pi/L}. \tag{16b}$$

Here i is the imaginary unit, ρ is the radius of a circle in the domain of analyticity. The function γ is the quotient of characteristic polynomials of the underlying multi-step method, and is taken as [22, 23]

$$\gamma(z) = 3/2 - 2z + z^2/2. \tag{17}$$

In addition, $\hat{G}$ and $\hat{H}$ utilized in Eq. (16) are the 2D Laplace-domain fundamental solutions, which are defined with Laplace parameter s as [32]

$$\hat{G}(r,s) = 2K_0(sr), \tag{18a}$$

$$\hat{H}(r,s) = \frac{\partial \hat{G}}{\partial \mathbf{n}}(r,s) = -2sK_1(sr)\frac{\partial r}{\partial \mathbf{n}}, \tag{18b}$$

where K_0 and K_1 are the second kind modified Bessel functions of zero and first order respectively, and $\partial/\partial\mathbf{n}$ is a partial derivative with respect to the outward normal direction on $\mathbf{y}$.

Arranging Eq. (15) according to the boundary conditions, a recursion formula can be established:

$$\begin{aligned}&\sum_{j=1}^{M}\left[\frac{\delta_{\mathbf{x}\mathbf{y}_j}}{2} + \omega_0\left(\hat{H},\mathbf{x},\Delta t\right)\right] p_j(m\Delta t) - \sum_{j=1}^{M}\omega_0\left(\hat{G},\mathbf{x},\Delta t\right) q_j(m\Delta t) \\ &= \sum_{k=1}^{m-1}\sum_{j=1}^{M}\omega_{m-k}\left(\hat{G},\mathbf{x},\Delta t\right) q_j(k\Delta t) - \sum_{k=1}^{m-1}\sum_{j=1}^{M}\omega_{m-k}\left(\hat{H},\mathbf{x},\Delta t\right) p_j(k\Delta t) \\ &- \sum_{k=1}^{m}\sum_{s=1}^{N}\omega_{m-k}\left(\hat{G},\mathbf{x},\Delta t\right) a_s(k\Delta t).\end{aligned} \tag{19}$$

For a time step m, all the values before $m\Delta t$ on the right side of Eq. (19) are calculated and stored in previous steps, while the source term $a_s(m\Delta t)$ is obtained from DVM results at the actual time step. Then, it is necessary to solve the equation for unknown boundary data $q_j(m\Delta t)$ or $p_j(m\Delta t)$ at time step m.

Equation (19) can be written in a matrix form with all the unknown boundary values in the vector $\boldsymbol{\lambda}$,

$$A\boldsymbol{\lambda} = \mathbf{b}, \tag{20}$$

where A is the coefficient matrix and $\mathbf{b}$ is the known right-hand side vector. The computation of vector b requires $O((M+N)^2)$ work and the matrix inversion needs $O(M^2)$ operations once a time step in the conventional CQ-BEM approach. Therefore, a complicated problem with multiple boundary elements and numerous vortex particles cannot be solved directly. Besides the computation complexity, it is usually difficult to solve Eq. (20) due to the ill-conditioned coefficient matrix. Consequently, following Saitoh [33], the CQ-BEM is accelerated by the FMM in this study.

3.3. Time-Domain Fast Multipole BEM based on the CQM for 2D Wave Propagation

The FMM developed by Rokhlin and Greengard is a technique for reducing computational time and memory requirement in large-scale problem calculations [34]. Since the FMM and its applications to the

BEM have been described in detail in other published papers [35, 36], we will only summarize the essential formulas derived for 2D wave propagation here.

Considering a field point **x** and a source point **y** located in a polar coordinate system originating at the point **o** closer to **y**, as shown in Fig. 2. The fundamental solutions $\hat{G}$ and $\hat{H}$ can be expanded using Graf's addition theorem [37]:

$$\begin{aligned}&\omega_{m-k}\left(\hat{G},\mathbf{x},\Delta t\right)q_j\left(k\Delta t\right)\\&=\frac{\rho^{-m+k}}{L}\sum_{l=0}^{L-1}\hat{G}\left(\mathbf{x},\mathbf{y},\gamma\left(\frac{\rho e^{il2\pi/L}}{\Delta t}\right)\right)q_j\left(k\Delta t\right)e^{-i(m-k)l2\pi/L}\\&=\frac{2\rho^{-m+k}}{L}\sum_{l=0}^{L-1}\sum_{n=-\infty}^{\infty}K_n\left(s\cdot|\mathbf{x}-\mathbf{o}|\right)e^{in\theta}M_n\left(\mathbf{o}\right)e^{-i(m-k)l2\pi/L},\end{aligned}\tag{20a}$$

$$\begin{aligned}&\omega_{m-k}\left(\hat{H},\mathbf{x},\Delta t\right)p_j\left(k\Delta t\right)\\&=\frac{\rho^{-n}}{L}\sum_{l=0}^{L-1}\hat{H}\left(\mathbf{x},\mathbf{y},\gamma\left(\frac{\rho e^{il2\pi/L}}{\Delta t}\right)\right)p_j\left(k\Delta t\right)e^{-inl2\pi/L}\\&=\frac{2\rho^{-m+k}}{L}\sum_{l=0}^{L-1}\sum_{n=-\infty}^{\infty}K_n\left(s\cdot|\mathbf{x}-\mathbf{o}|\right)e^{in\theta}M_n'\left(\mathbf{o}\right)e^{-i(m-k)l2\pi/L},\end{aligned}\tag{20b}$$

where $|\mathbf{x}-\mathbf{o}|$ and θ are the radius and polar angle of the field point **x**. Note that the multipole moments M_n and M_n' on **o** are not any longer associated with **x**, and are given by

$$M_n\left(\mathbf{o}\right)=\sum_{j=1}^{n}I_n\left(s|\mathbf{y}-\mathbf{o}|\right)e^{-in\varphi}q_j\left(k\Delta t\right),\tag{21a}$$

$$\begin{aligned}M_n'\left(\mathbf{o}\right)&=\sum_{j=1}^{n}sI_{n-1}\left(s|\mathbf{y}-\mathbf{o}|\right)e^{-i\delta}p_j\left(k\Delta t\right)e^{-in\varphi}\\&+\sum_{j=1}^{n}sI_{n+1}\left(s|\mathbf{y}-\mathbf{o}|\right)e^{i\delta}p_j\left(k\Delta t\right)e^{-in\varphi}.\end{aligned}\tag{21b}$$

Similarly, $|\mathbf{y}-\mathbf{o}|$ and φ are the radius and polar angle of the source point **y**, I is the modified Bessel function of the first kind.

The center of multipole expansions can be shifted from **o** to **o'** according to a M2M translation,

$$M_\mu\left(\mathbf{o}'\right)=\sum_{n=-\infty}^{\infty}M_n\left(\mathbf{o}\right)I_{\mu-n}\left(s|\mathbf{o}-\mathbf{o}'|\right)e^{-i(\mu-n)\Psi},\tag{22}$$

where M_μ is the new multipole moment on **o'**, $|\mathbf{o}-\mathbf{o}'|$ and Ψ are the polar coordinate components of the original multipole center **o** based on the new expansion point **o'**.

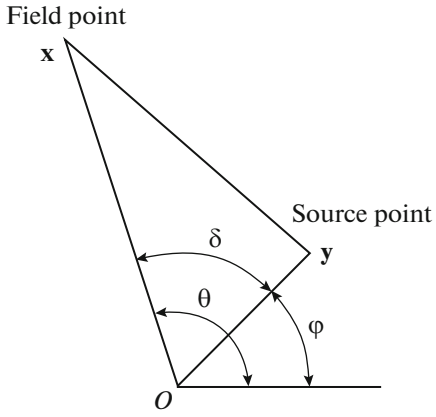

Fig. 2. Multipole expansion and Graf's addition theorem.

In addition, the source terms can also be calculated using a local expansion:

$$\begin{aligned}&\omega_{m-k}\left(\hat{G},\mathbf{x},\Delta t\right)q_j\left(k\Delta t\right)\\&=\frac{\rho^{-m+k}}{L}\sum_{l=0}^{L-1}\hat{G}\left(\mathbf{x},\mathbf{y},\gamma\left(\frac{\rho e^{il2\pi/L}}{\Delta t}\right)\right)q_j\left(k\Delta t\right)e^{-i(m-k)l2\pi/L}\\&=\frac{2\rho^{-m+k}}{L}\sum_{l=0}^{L-1}\sum_{\nu=-\infty}^{\infty}L_\mu\left(\mathrm{x}_1\right)I_\mu\left(s|\mathbf{x}_1-\mathbf{x}|\right)e^{-i\mu\alpha}e^{-i(m-k)l2\pi/L}.\end{aligned}\tag{23}$$

In Eq. (23), $|\mathbf{x}_1-\mathbf{x}|$ and α are the polar coordinate components of source point $\mathbf{x}_1$ based on the local expansion center **x**. And L_μ is the local expansion coefficient, which can be obtained from multipole moment by using a M2L translation,

$$\begin{aligned}&L_\mu\left(\mathbf{x}_1\right)\\&=\sum_{n=-\infty}^{\infty}\left(-1\right)^n M_n\left(\mathbf{x}_0\right)K_{\mu+n}\left(s|\mathbf{x}_0-\mathbf{x}_1|\right)e^{i(\mu+n)\beta},\end{aligned}\tag{24}$$

where $|\mathbf{x}_0-\mathbf{x}_1|$ and β are the radius and polar angle of the point $\mathbf{x}_0$ based on $\mathbf{x}_1$. The local expansion center can be shifted from **o'** to $\mathbf{x}_0$ using the following L2L formula:

$$\begin{aligned}&L_n\left(\mathbf{x}_0\right)\\&=\sum_{\mu=-\infty}^{\infty}\left(-1\right)^{\mu-n}L_\mu\left(\mathbf{o}'\right)I_{\mu-n}\left(s|\mathbf{o}'-\mathbf{x}_0|\right)e^{-i(\mu-n)\gamma},\end{aligned}\tag{25}$$

where L_n is the new local expansion coefficient. Moreover, $|\mathbf{o}'-\mathbf{x}_0|$ and γ are the polar coordinate components of the original local center **o'** based on the new expansion point $\mathbf{x}_0$.

4. ALGORITHM IMPLEMENTATION

A computer program to implement the method presented in the previous section is written in FORTRAN, which consists of two main components: flow field computation and far-field noise prediction. The

Table 1. Comparison of the elapsed time

Cases	CQ-BEM (HP)	CQ-FMBEM (HP)	CFD/FWH (DELL)
Circular cylinder	84.5 h	6.5 h	18.5 h
Square cylinder (case 1)	77.0 h	5.5 h	16.5 h
Square cylinder (case 2)	75.5 h	5.5 h	16.0 h

code begins by setting up the geometry, including calculation of the chord, profile slope, normal vector of each element and the coordinates of the vortex control points. The DVM procedure, constructed by four successive steps named vorticity generation, velocity computation, vortex convection as well as merging and elimination, is employed to simulate vortices producing on a solid surface, diffusing and convecting in the wake. The CQ-BEM program is used to calculate the radiated field from source points and the scattered field from a solid surface. Acoustic pressure is evaluated by the FMM on field points that are far away from the source points, and computed directly on those ones that are neighboring to the source points. An iterative solver, preconditioned GMRES method, is used to solve the system of equations for the unknown boundary quantities. The computational stages are as follows.

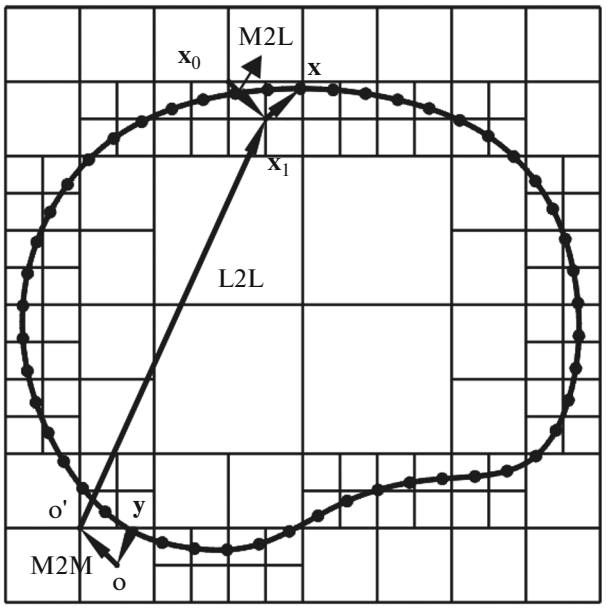

Fig. 3. Fast solution of 2D acoustic scattering problem based on the FMM.

Part I: flow field calculation.

Step 0. Initialization and data preparation. Initialize all the time-dependent variables. Choose the calculation precision ε, the order of multipole expansion p and the maximum number s of vortex particles allowed in a childless box for the FMM. Set the parameters L and R for the CQM.

Read in the nodes data of solid surface, then the straight-line elements can be obtained by joining successive data points. Length, profile slope, pivotal point and normal direction of each element are calculated and stored.

Step 1. Vorticity generation and shedding. Compute and invert the influence coefficients matrix. Loop on the center of boundary elements where the induced velocities are calculated and added together. The strengths of the vortex are then obtained by multiplying the inverted matrix by the column vector of local velocity. Then shed vortex particles at half local velocities at prescribed points.

Step 2. Viscous diffusion. The process of viscous diffusion, resulting in the vortices core growing and weakening in strength, is simulated by shifting all the discrete vortices with random displacements during each time step [28].

Step 3. Vortex convection. Calculate induced velocity at the point of each particle due to intermediate and free vortices. Then convect all the discrete vortices using an Euler explicit scheme according to Eq. (11).

Step 4. Merging and elimination. The vortices will be deleted if they penetrate the body. To keep the number of vortices reasonable, two vortices in close proximity are merged to satisfy the zeroth and first-order vorticity moment conservation. The position and circulation of the new vortex are given by

$$\mathbf{y}^* = \frac{\mathbf{y}_i\Gamma_i + \mathbf{y}_j\Gamma_j}{\Gamma_i + \Gamma_j}, \tag{26}$$

$$\Gamma^* = \Gamma_i + \Gamma_j. \tag{27}$$

Part II: Far-field noise computation.

Step 5. Build up a tree structure . To run the FMM algorithm, a hierarchical tree of boxes is constructed by dividing the 2D computational domain (a box containing all boundary elements and discrete vortices) into smaller and smaller sub-domains, as shown in Fig. 3.

Step 6. Upward pass. For each childless box b, calculate multipole moment at its center from all vortex particles in b using Eq. (21). Recursively move the moment from b's center to its parent's center by using M2M. Then, a p-th order multipole expansion is generated for each box at its center representing the contributions from all contained vortex particles.

Step 7. Downward pass. Compute local expansion coefficients for all boxes starting from level 2 to the lowest level:

(1) For each box b, the M2L translation is used to convert the multipole expansion of all boxes in its interaction list to a local expansion on b's center.

(2) Translate local coefficients of box b to b's children using the L2L translation.

The local expansions obtained in step 7 are added together for each childless box, representing the contributions due to all vortex particles in non-neighboring boxes.

Step 8. Evaluation of the integrals. Suppose a collocation point $\mathbf{y}_0$ is on an element (intermediate vortex) in childless box b.

(1) Calculate contributions from elements and particles contained in b and b's adjacent boxes directly according to Eq. (20).

(2) Compute contributions from boxes in b's interaction list and from those far separated from b by shifting the local expansion center to $\mathbf{y}_0$ using Eq. (23).

Step 9. Iterations of the solution. Initially, $\boldsymbol{\lambda}$ is chosen to be a zero vector. Then calculate $A\boldsymbol{\lambda}$ iteratively in the upward and downward pass with constantly updated $\boldsymbol{\lambda}$ vector until the residue of $\mathbf{b}$ reaches an acceptable tolerance.

5. NUMERICAL EXAMPLES

Numerical analyses are performed to confirm the ability of present method to accurately predict aeroacoustic sound with scattering effect from circular and square cylinders, since these problems have been extensively studied using other methods [38–40].

For each case, the cylinder is supposed to be rigid, that is $q = \partial p/\partial \mathbf{n} = 0$ on the surface. In the calculation of influence function γ, it is adopted $L = N = 128$ and $R = 0.922$, yielding an error of order $O(10^{-5})$ [41].

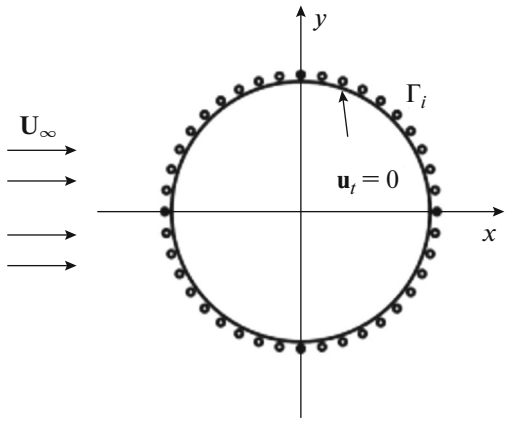

Fig. 4. Schematic diagram of flow over a circular cylinder.

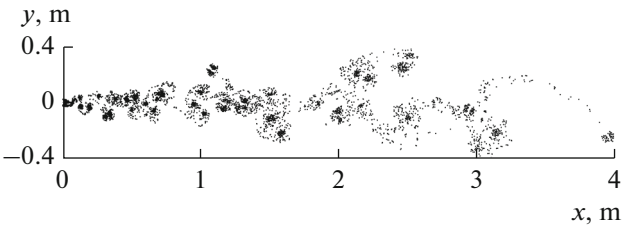

Fig. 5. Instantaneous flow pattern represented by vortex particles.

5.1. Aeroacoustic Sound from a Circular Cylinder

The schematic diagram of the flow model is provided in Fig. 4. A circular cylinder is fixed at the origin, and the horizontal and vertical coordinates are specified as x and y. The boundary condition of zero tangential velocity on the body surface $\mathbf{u}_t = 0$ is used to determine the surface vorticity.

For comparing with other experimental and computational works, the numerical simulation is conducted at Reynolds number $\mathrm{Re} = 9 \times 10^4$ based on an inflow velocity of $\mathbf{U}_\infty = 34.6$ m/s in the x direction and a cylinder diameter of $D = 0.038$ m. The working fluid is air with a density of $\rho = 1.225$ kg/m^3 and a dynamic viscosity of $\nu = 1.7894 \times 10^{-5}$ kg/m s. The boundary surface S of the cylinder is discretized into 180 constant elements. The vortices are advanced in time using the first order Euler scheme with a time step of 0.001 s.

5.1.1. Flow computation. Figure 5 shows the instantaneous flow pattern represented by vortex particles at time $T = |\mathbf{U}_\infty|t/D = 100$. At a high Reynolds number, the boundary layer is no longer stable showing an alternate vortex shedding and the evolution of the large-scale structures in the wake.

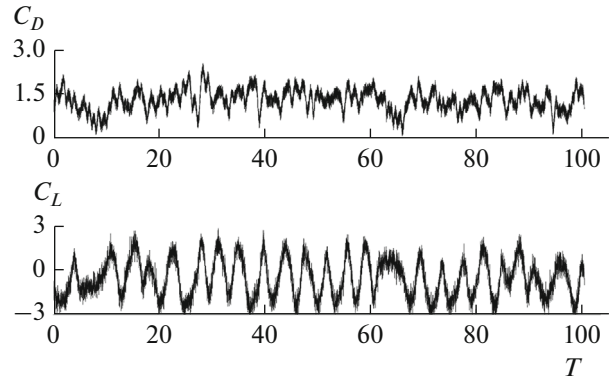

Fig. 6. Time histories of C_D and C_L on the circular cylinder.

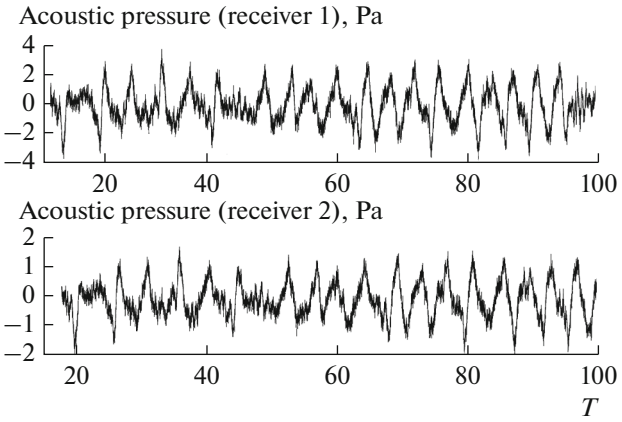

Fig. 7. Acoustic pressure at the receivers.

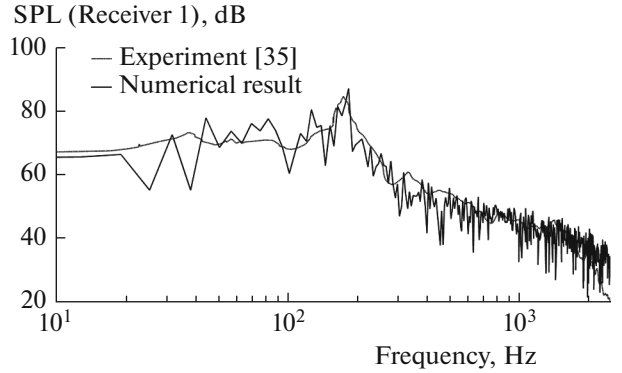

Fig. 8. Far-field acoustic spectra for the circular cylinder.

Figure 6 shows the time-histories of lift coefficient C_L and drag coefficient C_D. The computed average value of C_D is 1.317, which is larger than the experimentally measured value of 1.20 [38] by about 9.75%. The peak frequency of C_L is 184 Hz corresponding to a Strouhal number of $\mathrm{St} = fL/|\mathbf{U}_\infty| = 0.202$, which largely agrees with the experimental result St = 0.191.

5.1.2. Noise prediction. Figure 7 shows the instantaneous values of acoustic pressure at the receiver 1 and receiver 2 located at (0, 64D) and (0, 128D) respectively. Because both radiating and scattering effects decrease with distance, the sound pressure at receiver 1 is higher than that at receiver 2.

The aeroacoustic sound pressure level (SPL) in decibels (dB) predicted at the receivers 1 is provided in Fig. 8. It can be clearly seen that the far-field noise is broadband in nature, and the vortex shedding component is dominant in the spectrum. As shown in the figure, not only the peak frequency but also the amplitudes of broadband noise coincide with the experimental data. The peak SPL of 87.2 dB at receiver 1 is predicted at around 184 Hz, which is higher than the experimentally measured value of 84.7 by 2.5 dB [38]. The predicted overall sound pressure level (OASPL = 91.1 dB) at receiver 1 also agrees with the measured one (OASPL = 87.8 dB).

The SPL directivity at vortex shedding frequency f_0 is presented in Fig. 9. The maximum radiation direction is along the vertical direction when $f = f_0$, indicating that acoustic waves are generated in response to unsteady lift force acting on the cylinder surface and therefore have a dipolar nature.

5.2. Aeroacoustic Sound from a Square Cylinder

In this study, the flow of air around a 2D square cylinder is modeled, as shown in Fig. 10. The Reynolds number of $\mathrm{Re} = 2.4 \times 10^4$ (case 1) and 1.0×10^5 (case 2) are adopted, with inflow velocity $\mathbf{U}_\infty = 35$ (case 1) and 49 m/s (case 2) along the positive x axis. The square cylinder surfaces with side length $B = 0.01$ m (case 1) and 0.03 m (case 2) are discretized into 164 constant elements. The corners of the cylinders are "chamfered" in such a way that the two panels at a vertex are replaced by smaller elements to avoid numerical problems.

Figure 11 shows the time development of flow structure around the square cylinder at time $T = 80$, represented by vortex particles. As in the previous simulation, the alternate vortices shed from the surface and give rise to a turbulent wake.

Figure 12 shows the time histories of acoustic pressure fluctuation at the observer points located at (0, 0.515 m) for case 1 and at (0, −1.4 m) for case 2.

Figure 13 shows that a dominant single peak is observed in the broadband noise spectra. From the figure, we learn that the velocity of flow determines how vortices shed from the surface and affects the spectral content. Therefore, reducing flow velocity has the effect of reducing peak frequency and magnitude

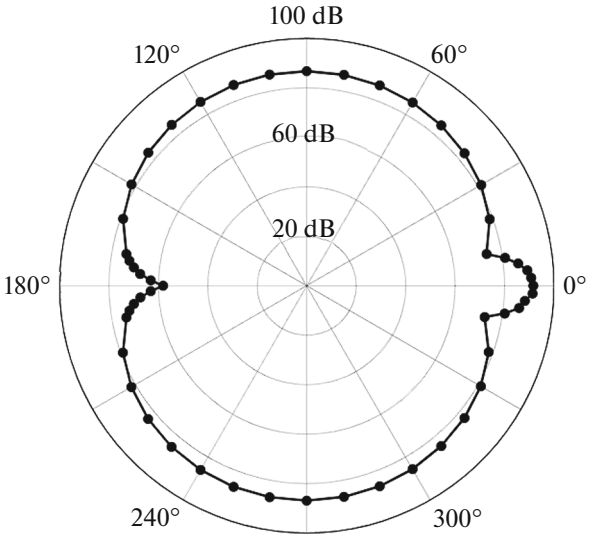

Fig. 9. Directivity pattern of SPL for the circular cylinder at the radial distance of $r = 128D$ when $f = f_0$.

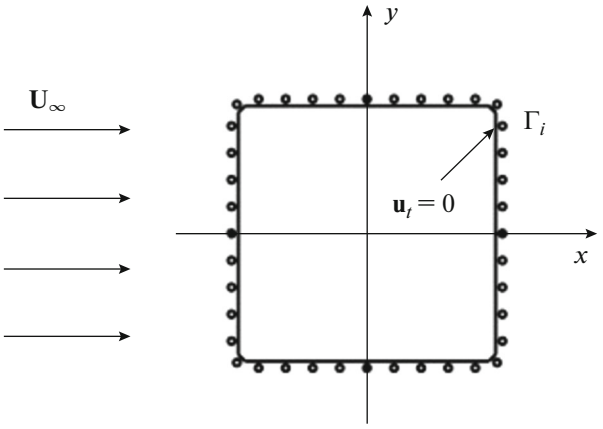

Fig. 10. Schematic diagram of flow over a square cylinder.

of a produced sound. The OASPL at the receivers are 91.7 (case 1) and 105.3 dB (case 2), which are consistent with the experimental results (91.4 and 101.5 dB) [39, 40], despite the fact that a double peak remains visible in the noise measurements.

Presented in Fig. 14 are the polar plots of SPL for the square cylinders. The directions of the maximum noise level are vertical when $f = f_0$, which confirms that the sound fields are dominated by a lift dipole. Moreover, the qualitative features of sound generation and propagation in the square cylinder cases are quite similar to those in the circular cylinder case.

In summary, all the analyses indicate that utilizing the numerical method for aeroacoustic noise prediction is feasible.

5.3. Computation Efficiency Comparison

The simulations were carried out on a PC (HP OPTIPLEX 380 with dual processors) and on a server computer (DELL R720 with 8 processors). The table shows the comparisons of elapsed time for the three approaches: CQ-BEM, CQ-FMBEM and CFD/FWH.

It is seen that the multipole algorithm becomes much faster than a traditional CQ-BEM, and the run time for CQ-FMBEM is about one third of that for CFD/FWH on the more powerful computer. Moreover, a much faster effect can be obtained by the CQ-FMBEM if the algorithm is optimized or a parallel computing code is applied.

6. CONCLUSIONS

A new method, combined with the DVM and CQ-FMBEM, for aeroacoustic noise prediction was proposed and applied to the calculations of far-field sound induced by airflow past cylinders. The accuracy and efficiency of the present method were confirmed by comparing our solutions with the reference results. The following conclusions were obtained.

(1) The DVM, used to compute a flow field at low Mach number, enables an efficient study of noise emission from the interaction between flow and bluff body.

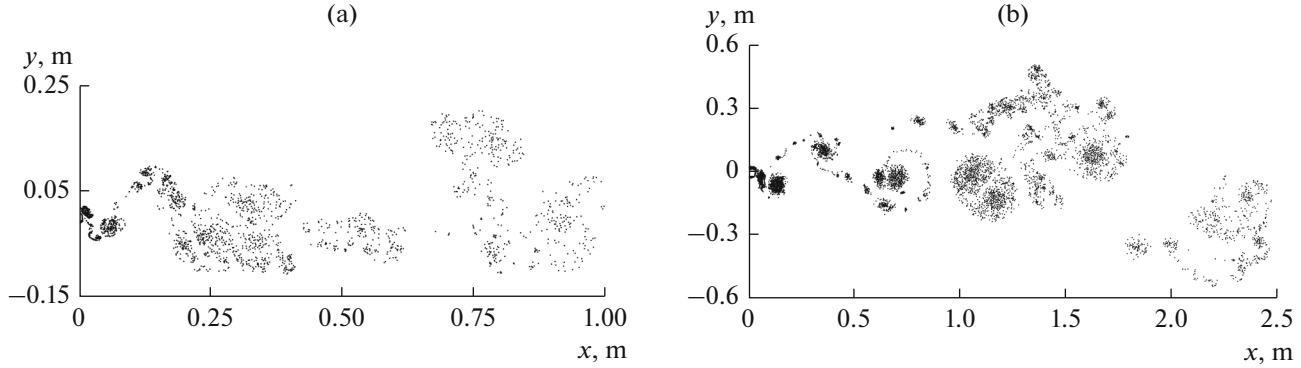

Fig. 11. Instantaneous flow pattern represented by vortex particles. (a) Case 1: $\mathbf{U}_\infty = 35$ m/s, B = 0.01 m, $\mathrm{Re} = 2.4 \times 10^4$; (b) case 2: $\mathbf{U}_\infty = 49$ m/s, B = 0.03 m, $\mathrm{Re} = 1.0 \times 10^5$.

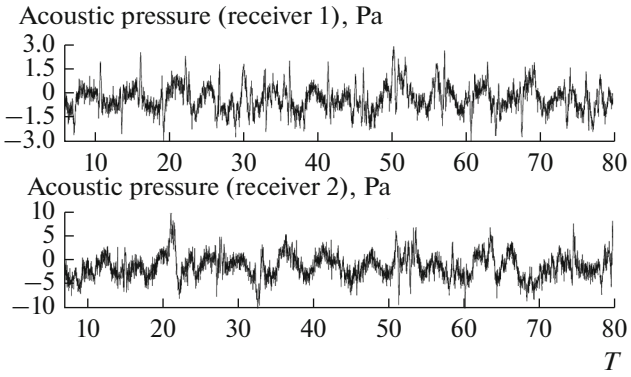

Fig. 12. Acoustic pressure at the receivers.

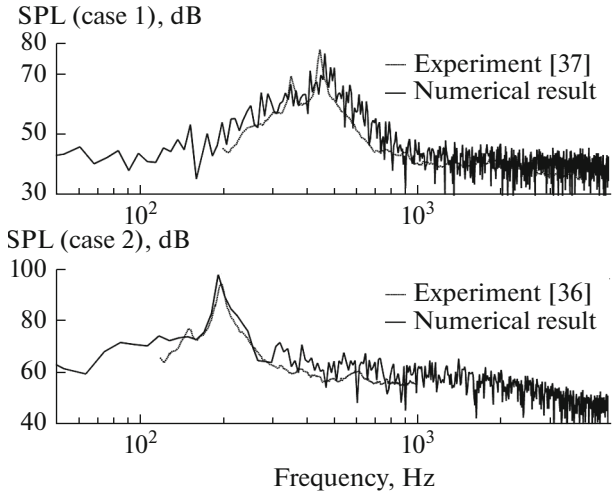

Fig. 13. Far-field acoustic spectra for the square cylinders.

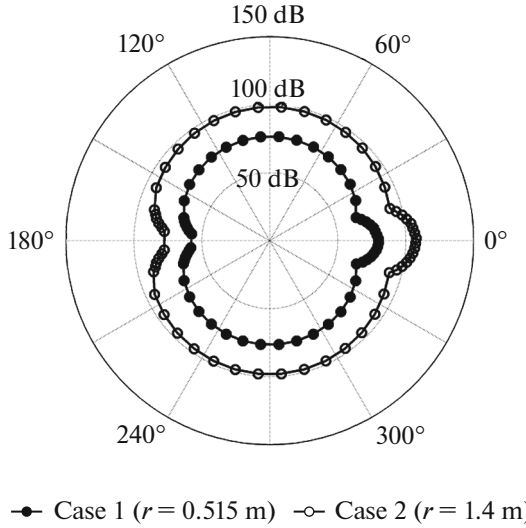

Fig. 14. Directivity pattern of SPL for the square cylinder when $f = f_0$.

(2) The time-domain BEM, employed to analyze the scattered sound wave from a solid surface, is capable of capturing broadband signals, thus especially suits for flow induced noise computation.

(3) The convolution integrals are performed utilizing the CQM, in which the weights depend only on a Laplace domain fundamental solution. In addition, this numerical scheme has a positive influence on the stability of the time stepping procedure.

(4) The boundary element equation is solved using an iterative method, which typically involves an enormous amount of matrix multiplications and requires too much computational time. The FMM is able to counter this low calculation efficiency problem of the conventional TDBEM.

ACKNOWLEDGMENTS

The research was supported by National Natural Science Foundation of China (51675262) and supported by the Project of National Key Research and Development Plan of China "New energy-saving environmental protection agricultural engine development" (2016YFD0700800) and the Advance research field fund project of China (6140210020116HK02001).

REFERENCES

1. V. F. Kopiev, M. Yu. Zaitsev, N. N. Ostrikov, S. L. Denisov, S. Yu. Makashov, V. A. Anikin, and V. V. Gromov, Acoust. Phys. **62**, 741 (2016).
2. Y. D. Khaletskiy and Y. S. Pochkin, Acoust. Phys. **61**, 101 (2015).
3. B. A. Singer and Y. Guo, Int. J. Comput. Fluid Dyn. **18**, 455 (2004).
4. K. Takeda and C. M. Shieh, Int. J. Comput. Fluid Dyn. **18**, 439 (2004).
5. F. Q. Hu, M. Y. Hussaini, and J. L. Manthey, J. Comput. Phys. **124**, 177 (1994).
6. C. Bogey and C. Bailly, J. Comput. Phys. **194**, 194 (2004).
7. E. Envia, A. G. Wilson, and D. Huff, Int. J. Comput. Fluid Dyn. **18**, 471 (2004).
8. C. Cheong, P. Joseph, Y. Park, and S. Lee, Appl. Acoust. **69**, 110 (2008).
9. M. Schlottkelakemper, F. Klemp, H. J. Cheng, A. Lintermann, M. Meinke, and W. Schröder, *Sustained Simulation Performance* (Springer, 2016).
10. S. C. Lo, G. Blaisdell, and A. Lyrintzis, Int. J. Aeroacoust. **11**, 783 (2013).
11. V. F. Kopiev, M. Yu. Zaytsev, V. I. Vorontsov, S. A. Karabasov, and V. A. Anikin, Acoust. Phys. **63**, 686 (2017).
12. I. Evers and N. Peake, J. Fluid Mech. **463**, 25 (2002).
13. P. R. Spalart and M. Shur, Aerosp. Sci. Technol. **1**, 297 (1997).
14. M. S. Howe, *Theory of Vortex Sound* (Cambridge Univ. Press, Cambridge, 2003).
15. M. S. Howe, J. Eng. Math. **41**, 367 (2001).

16. Z. C. Zheng, B. K. Tan, and Y. Xu, J. Appl. Math. **216**, 1072 (2010).
17. Y. Ogami and S. Akishita, Fluid Dyn. Res. **42**, 1 (2010).
18. O. A. Doronina, P. A. Bakhvalov, and T. K. Kozubskaya, Acoust. Phys. **62**, 467 (2016).
19. C. J. Zheng, H. F. Gao, L. Du, H. B. Chen, and C. Zhang, J. Comput. Phys. **305**, 677 (2016).
20. K. R. Pyatunin, N. V. Arkharova, and A. E. Remizov, Acoust. Phys. **62**, 495 (2016).
21. T. Maruyamaa, T. Saitohb, T. Q. Buia, and S. Hirosea, Comput. Methods Appl. Mech. Eng. **303**, 231 (2016).
22. C. Lubich, Numer. Math. **52**, 129 (1988).
23. C. Lubich, Numer. Math. **52**, 413 (1988).
24. A. Furukawa, T. Saitoh, and S. Hirose, Eng. Anal. Boundary Elem. **39**, 64 (2014).
25. T. Saitoh and S. Hirose, IOP Conf. Ser.: Mater. Sci. Eng. **10**, 012242 (2010).
26. M. J. Lighthill, Proc. R. Soc. A **267**, 147 (1962).
27. J. Chorin, J. Fluid Mech. **57**, 785 (1973).
28. R. I. Lewis, *Vortex Element Methods for Fluid Dynamic Analysis of Engineering Systems* (Cambridge Univ. Press, Cambridge, 1991).
29. J. H. Walther and A. Larsen, J. Wind Eng. Ind. Aerodyn. **67**, 183 (1997).
30. Y. Liu, *Fast Multipole Boundary Element Method*: *Theory and Applications in Engineering* (Cambridge Univ. Press, Cambridge, 2009).
31. I. Abreu, W. J. Mansur, and J. A. M. Carrer, Int. J. Numer. Methods Eng. **67**, 417 (2010).
32. R. Laliena and F. J. Sayas, Numer. Math. **112**, 637 (2009).
33. T. Saitoh, S. Hirose, and T. Fukui, Theor. Appl. Mech. Jpn. **57**, 385 (2009).
34. L. Greengard and V. Rokhlin, J. Comput. Phys. **737**, 325 (2012).
35. H. Isakari, T. Kondo, T. Takahashi, and T. Matsumoto, Comput. Methods Appl. Mech. Eng. **315**, 501 (2017).
36. N. A. Gumerov and R. Duraiswami, J. Acoust. Soc. Am. **141**, 3535 (2017).
37. W. Meng and L. Wang, Numer. Algorithms **72**, 91 (2016).
38. J. D. Revell, R. A. Prydz, and A. P. Hays, AIAA J. **16**, 889 (1978).
39. W. F. King and E. Pfizenmaier, J. Sound Vib. **328**, 318 (2009).
40. D. J. Moreau and C. J. Doolan, in *Proc. AIAA/CEAS 19th Aeroacoustics Conference* (Berlin, 2013), Vol. 135, p. 2406.
41. M. Schanz and H. Antes, Meccanica **32**, 179 (1997).